RSC Applied Polymers

ROYAL SOCIETY OF CHEMISTRY

PAPER

View Article Online
View Journal

Cite this: DOI: 10.1039/d6lp00028b

Phase morphology–structure–property–recyclability relationships of dynamically crosslinked thiol–ene photopolymers

Mengdi Chen,[a] Saleh Alfarhan,[a] Reyna Stockwell[a] and Kailong Jin *[a,b]

Thiol–ene photopolymerization provides a versatile platform for constructing dynamic covalent adaptable networks through the incorporation of reversible or exchangeable bonds. However, in such dynamic thiol–ene photopolymers, the influence of phase separation on network properties remains poorly understood. In this study, dynamic thiol–ene photopolymer networks with distinct phase morphologies are prepared by photocuring nonpolar polybutadiene (PBD) with polar disulfide-containing dithiol oligomers (Thioplast G4). When mixed in the bulk state, PBD and G4 mixtures undergo phase separation due to their pronounced polarity mismatch, and subsequent photocuring yields morphologically heterogeneous networks comprising a PBD-rich continuous phase and G4-rich dispersed domains (noted as X series). In stark contrast, the addition of tetrahydrofuran leads to fully dissolved PBD/G4/tetrahydrofuran precursor mixtures, and subsequent photocuring in the solution state produces morphologically homogeneous, optically transparent networks (noted as HX series). Despite their identical PBD and G4 compositions in feed precursor mixtures, X and HX series exhibit pronounced differences in thiol–ene conversion, optical transparency, thermal transitions, mechanical extensibility, and chemical deconstruction kinetics. Across the varying G4 loadings employed to modulate crosslink density, these direct X and HX comparison results demonstrate how phase morphology can be tailored to tune the structure, property, and recyclability of thiol–ene photopolymer networks comprising dynamic disulfide bonds.

Received 27th January 2026,
Accepted 9th April 2026

DOI: 10.1039/d6lp00028b

rsc.li/rscapplpolym

1. Introduction

Thiol–ene photopolymerization provides a versatile platform for fabricating crosslinked polymer networks, due to its step-growth reaction mechanism,[1–3] high conversion,[3,4] reduced shrinkage stress,[2–5] and tolerance to oxygen inhibition.[3,6–8] Compared to conventional chain-growth (meth)acrylate photopolymerization, thiol–ene reactions can form more uniform networks with controlled crosslink density,[2,4,9,10] making them attractive for applications ranging from coatings and adhesives to optical materials and additive manufacturing.[11–16] Beyond permanently crosslinked networks, thiol–ene photopolymerization is highly compatible with dynamic covalent chemistry through the incorporation of reversible or exchangeable bonds, such as Diels–Alder,[17–19] thioester,[13,20–26] disulfide linkages,[27–33] transesterification,[34,35] reversible boronic ester,[36,37] and enamine-based exchange.[38] These dynamic bonds enable bond exchange, network rearrangement, and chemical deconstruction under appropriate conditions, thereby enabling reprocessability and extending material lifetime.

Most reported dynamic thiol–ene photopolymer systems rely on synthetically demanding molecular designs that pre-install dynamic functionalities into photo-reactive monomers or crosslinkers, which may limit scalability and practical implementation.[13,24] To address this challenge, we previously introduced a simple one-step photopolymerization strategy to construct disulfide-containing dynamic thiol–ene networks by directly reacting multifunctional alkenes with Thioplast G4, a liquid polysulfide oligomer bearing multiple internal disulfide bonds and terminal reactive thiols.[28] The resulting networks can be completely deconstructed *via* thiol–disulfide exchange into thiol-terminated oligomers, which can be reused to construct next-generation thiol–ene photopolymer networks with nearly identical chemical compositions and thermomechanical properties over multiple recycling cycles.[28] Building on this platform, we further demonstrated that crosslinking chemistry and degradability can be programmed by controlling the wavelength-selective photopolymerization pathways (*i.e.*, thiol–acrylate addition reaction *vs.* acrylate homopolymerization) in a thiol–acrylate system, producing networks with fundamentally different crosslinking architectures and deconstructability from identical precursor formulations.[29] More recently, we

[a]*Chemical Engineering, School for Engineering of Matter, Transport and Energy, Arizona State University, Tempe, AZ 85287, USA. E-mail: kailong.jin@asu.edu*
[b]*Biodesign Center for Sustainable Macromolecular Materials and Manufacturing, Arizona State University, Tempe, AZ 85287, USA*

incorporated crystallizable segments into these disulfide-containing dynamic thiol–ene photopolymers, resulting in semicrystalline morphologies with coexisting crystalline and amorphous domains and significantly enhanced thermomechanical performance while preserving chemical recyclability.[30] Notably, in our previous studies,[28–30] all these disulfide-containing dynamic thiol–ene photopolymer networks were prepared using homogeneous precursor formulations, and the influence of phase separation has not been studied.

Phase separation is a common structural/morphological feature in crosslinked polymers, which plays a critical role in determining mechanical, thermal, and transport properties.[39–45] By creating heterogeneous morphologies with coexisting hard and soft domains, phase separation offers additional control over stiffness, toughness, and relaxation behavior beyond network chemistry.[45–50] In covalent adaptable networks (CANs) such as vitrimers,[45,50–56] phase separation is particularly important because the reversible/exchange reactions among dynamic bonds and thus network properties are highly sensitive to spatial heterogeneity. For example, Han *et al.*[51] studied the phase separation between dynamic epoxy-based vitrimer phases and static PMMA phases in vitrimer/PMMA hybrid systems at varying compositions. They observed that the stress relaxation time increased from ~3 h at 0 wt% PMMA to ~10 h at 50 wt% PMMA, where excessive PMMA induced a phase-separated morphology that spatially isolated the vitrimer domains and restricted the accessibility of transesterification reactions. As a result, the redistribution of network connectivity and thus stress relaxation were hindered.[51] Despite these advances, systematic studies on photopolymerized dynamic networks with phase-separated morphologies remain limited, highlighting the need to better understand and exploit phase separation as an independent material parameter to design mechanically robust yet chemically recyclable thiol–ene photopolymers.

In this study, we induce phase separation in dynamic thiol–ene photopolymers by reacting polybutadiene (PBD), a nonpolar polymer comprising reactive carbon–carbon double bonds, with Thioplast G4, a more polar disulfide-containing oligomer comprising reactive terminal thiols. The pronounced polarity mismatch between PBD and G4 leads to phase-separated precursor mixtures, and subsequent photocuring in the bulk state produces morphologically heterogeneous networks with a PBD-rich continuous phase and G4-rich dispersed domains. In stark contrast, the addition of tetrahydrofuran (THF) leads to fully dissolved PBD/G4/THF precursor mixtures, and subsequent photocuring in the solution state and drying produces morphologically homogeneous PBD–G4 networks. A direct comparison between these two series of PBD–G4 networks, *i.e.*, phase-separated (noted as X series) *vs.* homogeneous (or phase-mixed, noted as HX series), both of which are prepared using precursor mixtures at identical PBD and G4 compositions, elucidates the effects of phase separation on their structure–property–recyclability relationships. In addition, we systematically control the crosslink density by varying the G4 contents in these PBD–G4 networks to understand the interplay between phase separation and crosslink density. Specifically, we systematically compare the thiol–ene reaction conversion, optical appearance, phase morphology, thermomechanical performance, and deconstruction behavior of both X and HX series of PBD–G4 networks. Collectively, this study establishes phase morphology as a powerful and independent design parameter, beyond chemical composition alone, for tuning the material properties of dynamic thiol–ene photopolymer networks, while preserving their chemical deconstruction capabilities.

2. Experimental

2.1. Materials and methods

2.1.1. Materials. Polybutadiene (PBD), with a number-average molecular weight $M_n \approx 5000$ g mol^{-1}, was purchased from Sigma-Aldrich and used as received. PBD contains unsaturated carbon–carbon double bonds originating from both 1,4-addition (*i.e.*, double bond within the main chain) and 1,2-addition (*i.e.*, vinyl group dangling from the main chain), with the relative content of 1,4- to 1,2-unsaturation being ~88% to ~12% (see SI for details). A simple calculation indicates that 1 mole of such PBD chains contain on average ~81 moles of main-chain double bonds and ~11 moles of side-chain vinyl groups. Thioplast G4 (with a weight-average molecular weight $M_w \approx 980$ g mol^{-1}), a difunctional thiol oligomer containing approximately 5 dynamic disulfide bonds on average per molecular backbone,[29] was generously provided by Nouryon and used as received. 2-(2-Methoxyethoxy)ethanethiol (ME, 97%), a monofunctional thiol, was purchased from Sigma-Aldrich and used as received. Photoinitiator, Omnirad 2100, was kindly donated by IGM Resins and used as received. Tetrahydrofuran (THF, 99%) and toluene (99.5%) were purchased from Oakwood Chemical and used as received for preparing homogeneous precursor solutions and gel fraction tests, respectively. Triethylamine (TEA, ≥99.5%) was purchased from Sigma-Aldrich and used as the base catalyst of the decrosslinking process. Deuterated chloroform ($CDCl_3$-d, 99.8%, contains 0.03% (v/v) TMS) was purchased from Sigma-Aldrich and used as received. Filter Paper (9.0 cm) was purchased from VWR and used as received.

2.1.2. Preparation of phase-separated *vs.* phase-mixed PBD–G4 networks. Phase-separated (X series) *vs.* phase-mixed (HX series) PBD–G4 thiol–ene networks were prepared *via* UV-induced photopolymerization. For phase-separated X series, PBD and G4 at various compositions were directly mixed, without adding any solvents, using a speed mixer (Hauschild SpeedMixer, DAC 150.3 FVZ) at 1500 rpm for 5 min, resulting in macroscopically phase-separated, optically translucent photoresin mixtures. For phase-mixed samples, THF was added at 2.5 times the total mass of PBD and G4, and the mixture was homogenized using a vortex mixer to produce homogeneous and transparent photoresin solution mixtures. For all these formulations, 1 wt% Omnirad 2100 photoinitiators (relative to the total mass of the entire photoresin

Table 1 Compositions of the phase-separated (X series) *vs.* phase-mixed (HX series) PBD–G4 photoresin formulations employed in this study, which contain varying PBD : G4 molar ratios

Sample name	Molar ratio [PBD] : [G4]	Mass ratio PBD : G4	THF amount	Photoinitiator loading	Visual appearance
X0.5	1 : 0.50	1 : 0.098	—	1 wt%	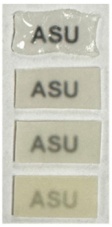
X0.75	1 : 0.75	1 : 0.147			
X1	1 : 1.00	1 : 0.196			
X2	1 : 2.00	1 : 0.392			
HX0.5	1 : 0.50	1 : 0.098	250 wt%	1 wt%	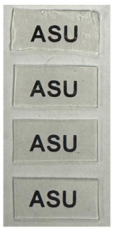
HX0.75	1 : 0.75	1 : 0.147			
HX1	1 : 1.00	1 : 0.196			
HX2	1 : 2.00	1 : 0.392			

mixture, both with and without THF) were added. The photoresin formulations prepared at different PBD : G4 molar ratios in this study are compiled in Table 1.

The photoresin mixtures were then poured and sandwiched between two clear glass slides separated by 1 mm-thick spacers, followed by UV irradiation using an Omnicure s1500 light source equipped with a 329–500 nm filter at an intensity of 10 mW cm^{-2} for 5 min on each side. After curing, the phase-separated samples were removed from the glass slides and characterized directly without further treatment. The resulting macroscopically phase-separated networks were opaque, with sample transparency decreasing as G4 loading increases (Table 1). In contrast, the THF-containing phase-mixed samples were first dried in a fume hood overnight under ambient conditions and further dried under dynamic vacuum at 40 °C for at least 4 h to fully remove any residual solvent. The resulting phase-mixed networks were almost fully transparent, and no obvious differences in transparency were observed across different compositions (Table 1).

2.1.3. Decrosslinking of dynamically crosslinked thiol–ene films *via* thiol–disulfide exchange reactions. Control decrosslinking experiments were first conducted on the X0.5 sample at 70 °C using three conditions: G4 only (X0.5 : G4 = 1 : 1 by mass), TEA only (X0.5 : TEA = 1 : 2 by mass), and a combined treatment using G4 and TEA was applied, with a mass ratio of X0.5 : G4 : TEA = 1 : 1 : 2. For each control experiment, ~0.25 g of X0.5 was placed in a 20 mL vial and swollen with excess toluene. Complete decrosslinking was achieved within ~1 week under the combined G4 and TEA treatment, whereas G4 and TEA alone resulted in partial and negligible deconstruction after ~1 month, respectively.

Subsequently, decrosslinking experiments were performed on all phase-separated and phase-mixed PBD–G4 networks in the presence of both G4 and TEA, with the mass ratios of X0.5 : G4 : TEA = 1 : 1 : 2, X0.75 : G4 : TEA = 1 : 1.5 : 3, X1 : G4 : TEA = 1 : 2 : 4, and X2 : G4 : TEA = 1 : 4 : 8. Typically, ~0.25 g of dynamically crosslinked PBD–G4 samples were placed in a 20 mL glass vial and mixed with G4 as decrosslinking regent, TEA as a base catalyst, and excess toluene as the swelling solvent to facilitate the penetration of decrosslinking agents, *i.e.*, G4, into crosslinked PBD–G4 networks. The resulting mixture was heated to 70 °C to trigger thiol–disulfide exchange reactions between G4 and crosslinked PBD–G4. After heating at 70 °C for approximately one week, a homogeneous, transparent solution was obtained, indicating the complete deconstruction of X0.5. Notably, the same added G4-to-sample and added TEA-to-sample ratios were applied to the corresponding HX0.5-HX2 samples to ensure a direct comparison between phase-separated and phase-mixed PBD–G4 networks.

2.2. Characterizations

2.2.1. Gel fraction determination by swelling test. The gel fractions of both phase-separated (opaque) and phase-mixed (transparent) PBD–G4 network samples, except X0.5, were determined by solvent swelling/extraction experiments in toluene at 70 °C to remove soluble components (*i.e.*, sol fractions). Typically, ~0.10 g of a crosslinked sample was placed in a 20 mL glass vial, followed by the addition of ~20 mL of toluene. The sample was allowed to swell at 70 °C for 24 h, after which the solvent was carefully extracted without removing any swollen sample and then replaced with fresh toluene. This swelling/extraction process was repeated three times for each sample to ensure complete removal of soluble fractions. After extraction, the swollen samples were air-dried in a fume hood overnight and subsequently vacuum-dried at 80 °C for 24 h to remove residual solvent. The gel fraction was calculated by comparing the mass of the dried sample after extraction with the original sample mass before swelling.

For the X0.5 sample with the lowest crosslink density, solvent swelling led to small, fragmented pieces, making sub-

sequent toluene extraction difficult. Instead, Soxhlet extraction was employed to determine its gel fraction. Specifically, ~0.25 g of X0.5 was sealed in a filter paper bag, which allowed toluene to penetrate and dissolve/extract the sol fractions while retaining solid fragments (*i.e.*, gel fractions) during extraction. Toluene was refluxed at 140–145 °C, and continuous extraction was carried out for 24 h. The retained insoluble fragments were then dried to determine the gel fraction using the same procedure described above. For all these samples, three independent specimens were tested, and the reported gel fraction values represent their averages with corresponding standard deviations.

2.2.2. Proton nuclear magnetic resonance (^{1}H NMR). The ^{1}H NMR spectra of PBD, ME, and PBD–ME systems were recorded using a Bruker Avance NEO 500 MHz spectrometer. PBD–ME samples with PBD : ME molar ratios of 1 : 1 and 1 : 5 were analyzed both before and after UV-induced photopolymerization to monitor changes in both alkene- and thiol-related resonances. All samples were prepared in $CDCl_3$-d, which contains tetramethylsilane (TMS) as an internal standard. The reported chemical shifts were referenced to TMS at 0.00 ppm.

2.2.3. Attenuated total reflectance Fourier transform infrared spectroscopy (ATR-FTIR). ATR-FTIR spectra of the bulk photoresin formulation before UV curing and the cross-sections of both phase-separated and phase-mixed network samples after UV curing were collected using a Nicolet Summit X spectrometer. Each spectrum was acquired by averaging 64 scans over a wavenumber range of 4000–400 cm^{-1}.

2.2.4. Photo-rheological measurements. Photo-rheological measurements were performed using a Discovery HR-30 rheometer equipped with a UV-curing accessory and a 20 mm diameter parallel-plate geometry that allowed UV light to pass through the sample. An Omnicure s2000 lamp coupled with a light guide was used as the UV light source to ensure uniform irradiation during photopolymerization. All measurements were conducted with a gap of 0.5 mm, a strain amplitude of 0.1%, and a frequency of 1 Hz. For the control experiment, neat PBD containing 1 wt% photoinitiator was loaded onto the rheometer, and a 15 s pre-shear was applied prior to UV exposure to establish a stable baseline, followed by UV irradiation at an intensity of 10 mW cm^{-2}. For the bulk phase-separated PBD : G4 = 1 : 0.5 photoresin precursor, the same rheological geometry and UV irradiation conditions were employed. In this case, a 30 s pre-shear was applied before UV exposure to ensure uniform sample contact and baseline prior to photopolymerization.

2.2.5. Differential scanning calorimetry (DSC). DSC measurements were performed on a TA DSC250 instrument under a nitrogen atmosphere to determine glass transition temperature (T_g). Typically, ~5 mg of each sample was sealed in an aluminum pan. To erase thermal history, the sample was first heated to 100 °C at a rate of 10 °C min^{-1} and held isothermally for 1 min, followed by cooling to −120 °C at the same rate and equilibrating isothermally for an additional 1 min. The sample was then reheated to 100 °C at a heating rate of 10 °C min^{-1}, and T_g was determined from the step change in heat flow during the second heating ramp.

2.2.6. Determination of tensile properties. Tensile tests of both phase-separated and phase-mixed PBD–G4 network films, except X0.5 were performed on an Instron 3343 instrument equipped with a 100 N load cell. Dog bone-shaped specimens were prepared in accordance with the ASTM-D638-V standard, with dimensions of 63.5 × 3.18 × ~1 mm for phase-separated samples and 63.5 × 3.18 × ~0.66 mm for phase-mixed samples. Tensile measurements were conducted at room temperature with a constant crosshead speed of 5 mm min^{-1}. For each composition, tensile tests were repeated five times, and the reported values represent their averages with standard deviations.

2.2.7. Rheological measurements. Oscillatory frequency-dependent rheological measurements were performed using a Discovery HR-30 rheometer equipped with an 8 mm diameter parallel-plate geometry, providing complementary insight into network integrity and viscoelastic response. Before testing, all samples were cut into disk-shaped specimens with a diameter of 8 mm. Before frequency sweep measurements, strain amplitude sweeps with strain from 0.1 to 10% at an angular frequency of 1 rad s^{-1} were conducted for all samples to identify the linear viscoelastic region (LVR). Based on these measurements, a strain amplitude of 1%, well within the LVR for all formulations, was selected for subsequent frequency sweeps to ensure that the measured moduli reflect intrinsic network properties rather than nonlinear deformation effects. Consequently, the storage modulus (G') and loss modulus (G'') were recorded during frequency sweep measurements conducted over an angular frequency range of 100 to 0.1 rad s^{-1} at room temperature under a strain amplitude of 1% (within the LVR). An axial compression of 0.1% was applied to ensure good contact between the sample and the plates.

2.2.8. Dynamic mechanical analysis (DMA). DMA experiments were performed using a Discovery DMA850 instrument to evaluate thermomechanical properties. Rectangular specimens were prepared for testing, with dimensions being ~20 × 5 × 1 mm for the phase-separated sample and ~20 × 5 × 0.66 mm for the phase-mixed sample. The measurements were conducted with a preload force of 0.01 N. Each sample was first equilibrated at −150 °C, well below its T_g, for 5 min. Temperature-dependent oscillatory measurements were then carried out from −150 to 100 °C at a heating rate of 3 °C min^{-1}, using a strain amplitude of 0.1% and a frequency of 1.0 Hz. Stress relaxation experiments were performed using the same DMA850 instrument and specimen geometry to evaluate the time-dependent mechanical response of the photocured X2 and HX2 networks at room temperature. The tests were conducted under a constant tensile strain of 5%, and the stress was recorded as a function of time over a duration of 5 min.

2.2.9. Thermogravimetric analysis (TGA). TGA experiments were performed on a TA-SDT 650 instrument under a nitrogen atmosphere. ~5 mg of each cured sample was heated from 35 to 800 °C at a heating rate of 20 °C min^{-1}. The sample mass was normalized to 100% at 35 °C prior to analysis.

2.2.10. Scanning electron microscopy (SEM). SEM was employed to study the cross-sectional morphology of all cured PBD–G4 samples, including both phase-separated and phase-mixed networks, using a Phenom XL G2 SEM instrument. To prepare cross-sections, the samples were first cooled in liquid nitrogen and subsequently fractured under cryogenic conditions to expose fresh cross-sectional surfaces. The fractured specimens were then mounted onto SEM sample holders using conductive carbon tape. Prior to SEM imaging, a ~6 nm-thick gold layer was sputter-coated onto each sample. SEM observations were carried out on the prepared cross-sections to reveal the morphologies of these photocured samples.

3. Results and discussion

3.1. Photocuring of phase-separated *vs.* phase-mixed PBD–G4 thiol–ene photopolymers

Phase-separated PBD–G4 thiol–ene networks were synthesized by photocuring bulk mixtures of PBD (comprising both 1,4- and 1,2-carbon–carbon double bonds) and G4 (comprising both thiol terminal groups and internal disulfide bonds), in the presence of 1 wt% photoinitiators. Due to the pronounced polarity mismatch between PBD and G4, the photoresin formulations cured in bulk remained macroscopically phase-separated throughout photopolymerization (Scheme 1, left), yielding opaque samples, noted as X0.5, X0.75, X1, and X2 (Table 1). In contrast, when THF was introduced to fully dissolve both PBD and G4 prior to photocuring, homogeneous photoresin solutions were obtained. Subsequent photopolymerization in the solution state produced phase-mixed, transparent samples (Scheme 1, right), noted as HX0.5, HX0.75, HX1, and HX2 (Table 1). The photoresin formulations used to prepare both phase-separated X0.5–X2 and phase-mixed HX0.5–HX2 samples are compiled in Table 1, with all compositions defined by the molar ratios between G4 and PBD macromolecules (*e.g.*, the molar ratio between G4 and PBD is 0.5 : 1 for both X0.5 and HX0.5). For both X and HX series, the molar ratio between G4 and PBD varied between 0.5 : 1 and 2 : 1 to establish their composition–structure–property relationships.

We first examined the photopolymerization kinetics of a bulk photoresin mixture with a G4 : PBD molar ratio of 0.5 : 1 by *in situ* photo-rheological measurements under ambient conditions. Fig. 1a shows the evolution of the shear storage modulus (G') and shear loss modulus (G'') of the bulk X0.5 photoresin during UV irradiation at an intensity of 10 mW cm^{-2}. As irradiation proceeded, G' increased more rapidly than G'', with G' surpassing G'' after ~2.2 min. This crossover is commonly taken as the gel point, at which an infinite, percolated network first appears so that the material transitions from liquid-like to solid-like behavior.[28,57,58] As irradiation proceeded further, both G' and G'' reached their plateau after ~5 min, indicating that the photopolymerization had reached the highest attainable conversion under such curing conditions. Notably, control experiments showed that PBD alone, containing 1 wt% photoinitiators, exhibited negligible changes in G' and G'' after ~10 min UV irradiation under almost the same conditions, with G' remaining consistently lower than G'' and no crossover detected (Fig. S1). These confirm that UV irradiation of PBD alone does not lead to gelation, and that network formation in the X0.5 sample originates from the thiol–ene photopolymerization reactions between PBD and G4 rather than from radical-mediated reactions of PBD. It is also noteworthy that X0.5 exhibited the slowest gelation among all the formulations in this study, which can be attributed to its low initial G4 content and the reduced effective thiol group concentration arising from macroscopic phase-separation. Based on the photo-rheological study of this slowest-gelling X0.5 system, we selected a consistent curing protocol to cure all the formulations in this study, *i.e.*, 5 min

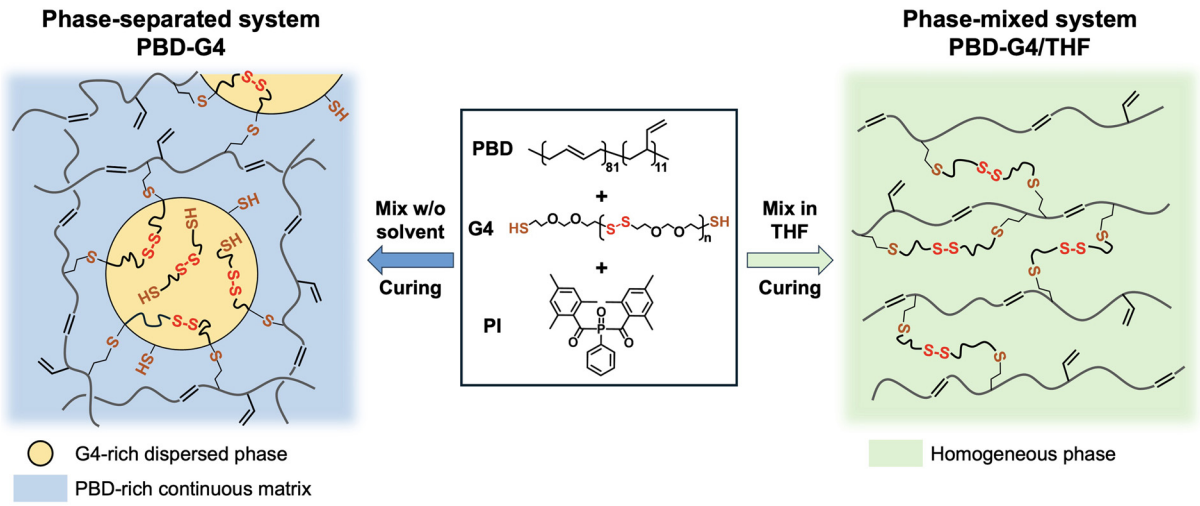

Scheme 1 Synthesis of phase-separated *vs.* phase-mixed PBD–G4 thiol–ene photopolymer networks containing dynamic disulfide bonds.

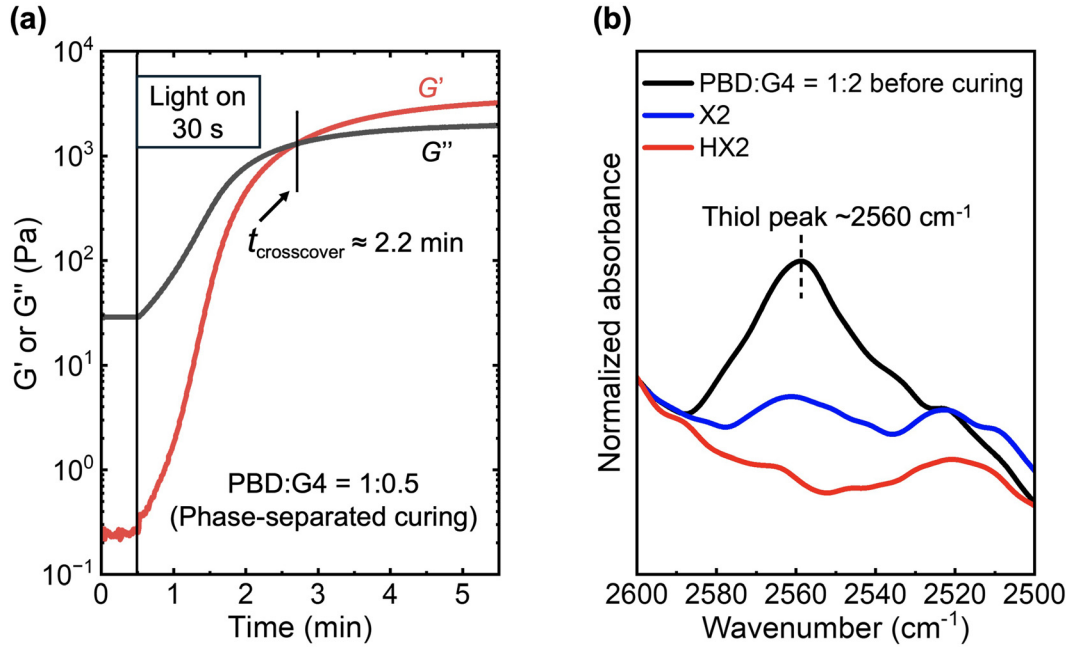

Fig. 1 (a) Photo-rheological analysis of the phase-separated X0.5 resin (PBD : G4 = 1 : 0.5) formulation under UV irradiation (*i.e.*, 10 mW cm^{-2}), showing the evolution of *G′* and *G″* over time; (b) ATR-FTIR spectra of the original photoresin (PBD : G4 = 1 : 2) before curing (black) and cured X2 (blue) and HX2 (red) samples.

UV exposure at an intensity of 10 mW cm^{-2} on each side of the film.

After photopolymerization, X0.5–X2 films (cured in the bulk state) exhibited thicknesses of ~1 mm and appeared opaque, with transparency decreasing with increasing G4 content (Table 1), indicative of their macroscopic phase-separated morphologies. In contrast, HX0.5–HX2 films (cured in the solution state) displayed thicknesses of ~0.66 mm after completely removing THF and were colorless and transparent, with no sign of macroscopic phase separation at varying G4 loadings. The rheological frequency scans of all these samples, regardless of phase-separated *vs.* phase-mixed, showed characteristics of crosslinked materials, with *G′* being much greater than *G″* at all frequencies and reaching a plateau at lower frequencies (Fig. S2), indicating the formation of elastically dominated, percolated crosslinked networks.[59,60]

ATR-FTIR was subsequently performed on the cross-sections, rather than the surfaces, of these photocured films. This approach minimizes surface effects and averages information across the film thickness, ensuring a more reliable determination of the overall functional group conversion after thiol–ene photopolymerization. Fig. 1b compiles the representative spectra of photocured X2 and HX2 samples as well as their precursor mixture PBD : G4 at a molar ratio of 1 : 2 before curing, highlighting the characteristic thiol group (–SH) absorption band at ~2560 cm^{-1} (Note: The ATR-FTIR spectra of all other X0.5–X1 and HX0.5–HX1 samples exhibited nearly invisible –SH peaks at ~2560 cm^{-1} both before and after curing, mainly due to a combination of low G4 loadings and the inherently weak –SH absorption at ~2560 cm^{-1}.)

According to Fig. 1b, the –SH peak at ~2560 cm^{-1} in the X2 sample decreased after photocuring with a noticeable residual peak, reporting an overall thiol conversion of ~60% in X2. In comparison, the –SH peak at ~2560 cm^{-1} almost disappeared in the HX2 sample after photocuring, reporting a nearly quantitative thiol conversion in HX2. This difference can be attributed to their distinct curing pathways: (a) In the macroscopically phase-separated X0.5–X2 systems, minority G4 components segregated into discrete G4-rich domains dispersed within the continuous PBD-rich matrix because of the thermodynamic incompatibility between G4 and PBD (Scheme 1, left). Under such conditions, thiol–ene reactions are spatially confined to the PBD/G4 interfaces, *i.e.*, only the thiol groups located at/near the surfaces of the dispersed G4-rich domains or a limited fraction of G4 dissolved within the PBD-rich continuous phase can effectively encounter and react with the carbon–carbon double bonds (*i.e.*, ene groups) on PBD chains. As a result, the thiol groups trapped inside the dispersed G4-rich domains would not react even after prolonged UV irradiation, resulting in a residual –SH peak at ~2560 cm^{-1} in X2 (Fig. 1b); (b) in the macroscopically phase-mixed HX0.5–HX2 systems, however, the addition of THF allowed homogeneous mixing of all reactive components at a molecular level prior to photocuring (Scheme 1, right). Under such conditions, thiol–ene reactions can achieve nearly quantitative conversion after photocuring in these phase-mixed systems (Fig. 1b), reporting consistently higher thiol group conversion than that observed in their phase-separated counterparts.

Table 2 compiles the determined gel fraction values for both phase-separated X0.5–X2 and phase-mixed HX0.5-HX2

Table 2 Gel fractions, thermal and mechanical properties of photocured PBD–G4 samples with (X0.5–X2) and without (HX0.5–HX2) macroscopic phase separation at varying compositions

Sample[a]	Gel fraction [%]	T_g [°C] (±1 °C)	G' [b] [MPa]	Young modulus[c] [MPa]	Tensile strength[c] [MPa]	Elongation at break[c] [%]
X0.5	27.1 ± 0.2	−90, −53	0.003 ± 0.002	—	—	—
X0.75	51.4 ± 0.5	−89, −53	0.024 ± 0.002	0.08 ± 0.01	0.12 ± 0.02	193 ± 21
X1	72.5 ± 0.5	−88, −54	0.070 ± 0.005	0.24 ± 0.01	0.19 ± 0.02	102 ± 16
X2	83.5 ± 0.2	−84, −57	0.294 ± 0.015	1.23 ± 0.02	0.44 ± 0.04	48 ± 5
HX0.5	63.2 ± 0.9	−86	0.009 ± 0.002	0.03 ± 0.01	0.05 ± 0.01	210 ± 26
HX0.75	79.0 ± 1.0	−84	0.036 ± 0.006	0.13 ± 0.01	0.09 ± 0.01	106 ± 4
HX1	84.7 ± 0.2	−81	0.084 ± 0.002	0.32 ± 0.01	0.15 ± 0.01	67 ± 2
HX2	93.0 ± 0.8	−73	0.234 ± 0.013	1.13 ± 0.03	0.33 ± 0.01	40 ± 2

[a] Reported errors are standard deviations from multiple measurements. [b] G' measured by rheometer at 0.1 rad s^{-1}. [c] Tensile properties measured at room temperature.

samples. According to Table 2, the gel fractions of both series increased with increasing G4 loadings, consistent with the increasing trend of G' plateau (a measure of crosslink density) at higher G4 loadings observed on their respective rheological frequency scans (Fig. S2). This is reasonable because an increased amount of G4 molecules, which serve as the crosslinkers for PBD, should promote network percolation and formation of an insoluble network structure. Notably, at the same G4 loadings, the phase-mixed series report consistently higher gel fraction values than those of their phase-separated counterparts, *e.g.*, the gel fraction values for HX2 *vs.* X2 and HX0.5 *vs.* X0.5 are 93.0 *vs.* 83.5 wt% and 63.2 *vs.* 27.1 wt%, respectively. The consistently higher gel fraction values in the phase-mixed series than their phase-separated counterparts can be attributed to their consistently higher thiol–ene reaction conversion when cured in the homogeneous solution state, as discussed above.

We further performed control experiments involving monofunctional thiol (*i.e.*, ME) and PBD to examine the relative reactivity between the 1,4-addition main-chain *vs.* 1,2-addition side-chain carbon–carbon double bonds in PBD toward thiol groups. Specifically, we compared the ^{1}H NMR spectra of PBD/ME mixtures (containing 1 wt% photoinitiators) before and after exposure to UV light irradiation under the same conditions (*i.e.*, 1 mm-gap between glass slides, 5 min irradiation at 10 mW cm^{-2} on each side; Fig. S3–S5). After photopolymerization, the proton signals associated with both 1,4-addition (peak a in Fig. S5) and 1,2-addition (peak b in Fig. S5) carbon–carbon double bonds decreased, indicating that they can both participate in thiol–ene reactions. Notably, the ratio between the integrals of the 1,4-alkene and 1,2-alkene protons (*i.e.*, a/b peak area ratio in Fig. S5) increased after photoreaction, demonstrating the preferential consumption of the 1,2-addition vinyl groups. A rough estimation in the Supplementary Information reports a reactivity ratio of ~14 : 1 between 1,2-alkenes and 1,4-alkenes toward thiols under the reaction conditions employed in this study. Such a higher reactivity of 1,2-addition vinyl groups is consistent with previous literature, which can be attributed to their greater conformational freedom and less steric hindrance than those of the 1,4-addition counterparts.[10]

3.2. Morphological properties of phase-separated *vs.* phase-mixed PBD–G4 networks

Fig. 2 shows the representative cross-sectional SEM images of both phase-separated X0.5–X2 (after photocuring) and phase-mixed HX0.5–HX2 (after photocuring and completely removing THF solvent) PBD–G4 samples, together with their respective digital photographs (same as those shown in Table 1). As shown in Fig. 2 (top row), the cross-sectional SEM images of X0.5–X2 samples demonstrate typical macroscopic phase-separated morphologies, where discrete, micron-sized G4-rich domains are randomly dispersed within a continuous PBD-rich matrix. At a relatively low G4 loading (*e.g.*, X0.5 with ~9 wt% G4), G4-rich domains are rather small (~2.8 μm) and sparsely distributed. As the G4 loading gradually increases to X2 with ~28 wt% G4, both the population and average size of G4-rich particles increase accordingly. The presence of these dispersed domains introduces significant heterogeneity and numerous interfaces into the network, leading to spatial variations in refractive index, enhanced light scattering, and a consequent loss of optical transparency.

In stark contrast, the cross-sectional SEM images of HX0.5–HX2 samples after photocuring and drying exhibit smooth fracture surfaces, with no sign of discernible phase boundaries between PBD and G4 at comparable magnifications. This indicates that THF effectively dissolved both PBD and G4 before photocuring, and subsequent homogeneous thiol–ene photopolymerization in the solution state led to the formation of single-phase PBD–G4 networks, with no sign of macroscopic phase separation even after removing THF. In these phase-mixed HX0.5–HX2 samples, the characteristic length scale of any compositional variation is well below the wavelength of visible light, resulting in minimal light scattering and optically transparent materials.

Beyond optical appearance, fundamental differences in their curing-induced network topologies arise from these two distinct photopolymerization pathways: (a) in the absence of THF (*i.e.*, phase-separated state), thiol–ene photopolymerization primarily occurs at phase boundaries (*i.e.*, interfaces), leading to incomplete and spatially heterogeneous incorporation of G4 into the final PBD–G4 network. Since a

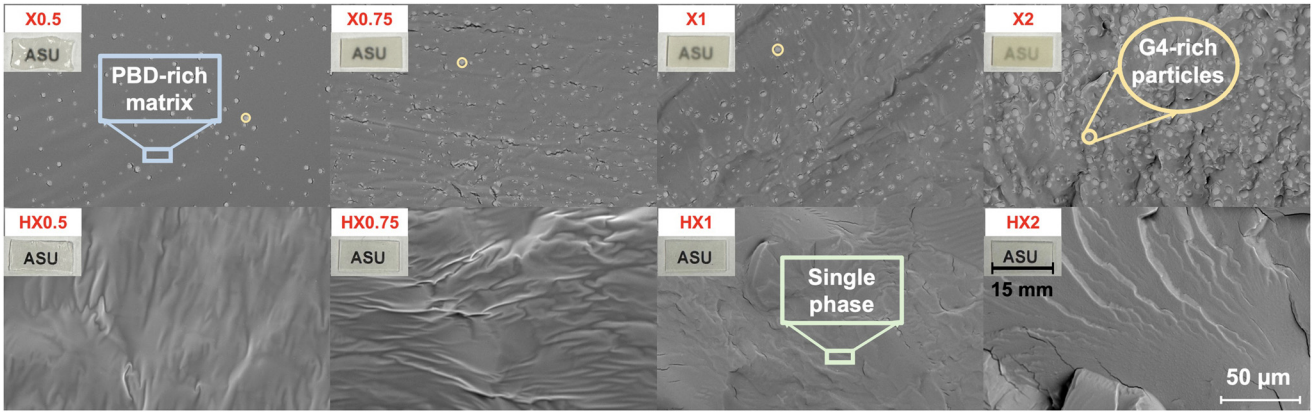

Fig. 2 Representative digital photographs and SEM images for photocured PBD–G4 samples at varying compositions, with (X0.5–X2) *vs.* without (HX0.5–HX2) macroscopic phase separation (areas marked with yellow circles are G4-rich dispersed domains and areas marked with blue boxes are PBD-rich matrix, respectively; areas marked with green boxes are the mixed single phase comprising both PBD and G4).

considerable amount of G4 molecules are trapped inside the dispersed G4-rich domains and thus would not participate in subsequent crosslinking reactions, these cured X0.5–X2 PBD–G4 samples failed to reach full conversion even after prolonged UV irradiation and reported relatively low gel fractions in the range of 27.1–83.5 wt%; (b) in the presence of THF (*i.e.*, phase-mixed state), PBD and G4 are molecularly mixed before photocuring, allowing thiol and ene functionalities to react more homogeneously throughout the material to reach nearly complete conversion. This leads to higher thiol conversion in HX0.5–HX2 and thus the formation of more fully developed PBD–G4 networks, with higher gel fractions in the range of 63.2–93.0 wt%. These marked morphological and topological differences between these two X and HX series directly impact their final material properties, which will be discussed in the following sections.

3.3. Thermal/mechanical properties of phase-separated *vs.* phase-mixed PBD–G4 networks

Fig. 3a compiles the DSC thermograms of both phase-separated X0.5–X2 and phase-mixed HX0.5–HX2 PBD–G4 networks, together with those of neat PBD and G4. For reference, neat PBD and G4 report a single T_g of ~−95 °C and ~−70 °C, respectively. Because of their phase-separated morphologies/structures, all X0.5–X2 network samples report two T_gs. For example, X2 reports a lower T_g at ~−84 °C (corresponding to the PBD-rich matrix) and another higher T_g at ~−57 °C (corresponding to the G4-dispersed domains). Both PBD- and G4-rich phases' T_gs are higher than those of neat PBD and G4 due to thiol–ene reactions, which increase the molecular weights and crosslinking constraints in both phases and thus reduce their segmental mobilities as compared to their neat counterparts. In stark contrast, all HX0.5–HX2 network samples appear to display a single, but broad glass transition because of their phase-mixed morphologies/structures, *e.g.*, T_g ~−73 °C for HX2. This broad T_g may be attributed to its relatively heterogeneous network structure, where a distribution of local compositions and crosslink constraints can lead to a broad spectrum of local segmental mobilities, even though it remains in the phase-mixed state.

To further support these DSC observations, we performed DMA experiments on both X2 and HX2 samples, which contain the highest G4 loading and thus possess the most pronounced potential for phase separation. As shown in Fig. 3b, the elastic tensile moduli (E') of X2 exhibit two stepwise decreases as temperature increases. Consistently, the tan δ (E'/E'' where E'' is the viscous tensile moduli) curve of X2 exhibits two distinct peaks in the tan δ curve, one centered around −60 °C (corresponding to the glass transition of the PBD-rich continuous phase) and the other centered around −16 °C (corresponding to the glass transition of the G4-rich dispersed phase). In contrast, the E' of HX2 exhibits a single stepwise decrease as temperature increases, and the corresponding tan δ curve exhibits a broad peak centered around −46 °C. Overall, these DMA results further confirm that phase-separated X networks contain two dynamically distinct phases, whereas phase-mixed HX networks comprise a single phase.

A closer look at the DSC results in Fig. 3a and Table 2 indicates that the difference between the two T_gs observed in X0.5–X2 decreases with increasing G4 content. For example, X0.5 reports two T_gs of ~−90 °C and ~−53 °C, while X2 reports two T_gs of ~−84 °C and ~−57 °C. In comparison, HX0.5–HX2 networks report a single T_g that increases with increasing G4 content. For example, HX0.5 reports a single T_g of ~−86 °C, while HX2 reports an increased single T_g of ~−73 °C. This increase in T_g for the HX series is because a higher G4 loading leads to increased crosslink density and gel fraction, thus reduced segmental mobility (see section 3.1 above).

Notably, at the same chemical compositions (*i.e.*, G4 loadings), the phase-mixed HX samples exhibit a single T_g that consistently locates between the two T_gs observed in the phase-separated X counterparts. This is consistent with the "T_g mixing rule" of miscible polymer blends,[61] whose T_g usually sits between the T_g values of its individual components. In our

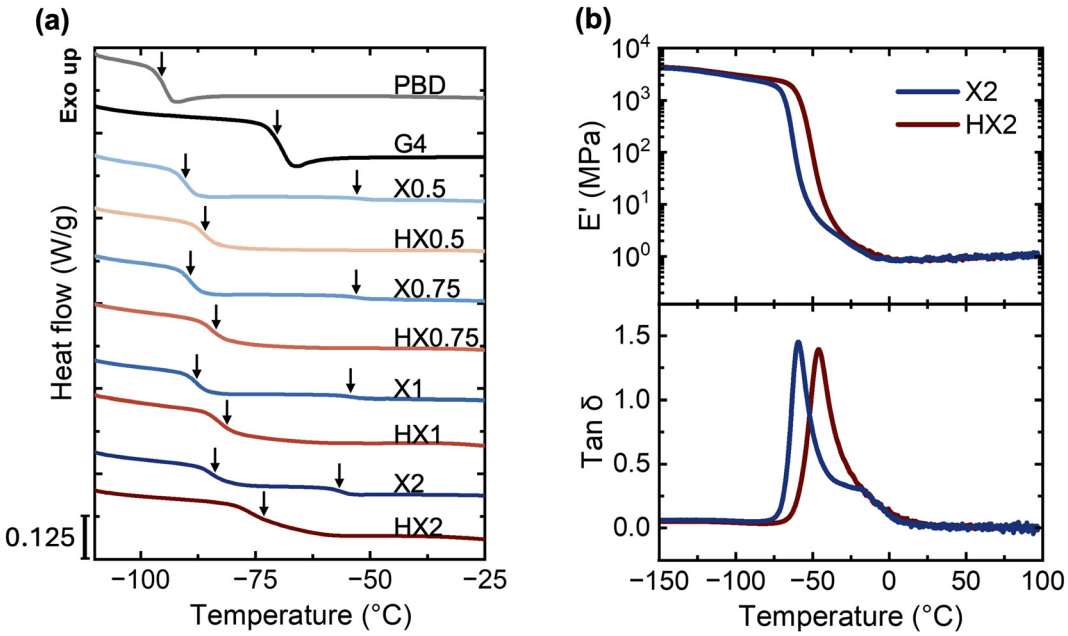

Fig. 3 (a) DSC thermograms of neat PBD, neat G4, and photocured PBD–G4 samples with (X0.5–X2) and without (HX0.5–HX2) macroscopic phase separation at varying compositions; (b) DMA temperature sweeps of X2 and HX2: E' *vs.* T (top) and tan δ *vs.* T (bottom). The arrows in (a) denote T_gs determined by DSC.

PBD–G4 network case, the PBD-rich phase represents the component with a higher mobility (thus lower T_g), whereas the G4-rich phase represents the other component with a lower mobility (thus higher T_g). The intermolecular chemical crosslinking induces phase-mixing between these two components, thus resulting in a single, intermediate "blend" T_g in these phase-mixed HX samples.

Interestingly, Fig. 3b shows that both X2 and HX2 exhibit nearly identical E' plateau values (~1 MPa) well above their T_gs in the rubber state, indicating that they possess similar effective crosslink densities as predicted by the ideal rubber elasticity theory. Similarly, all other X and HX networks show comparable crosslink densities at each G4 loading determined by the plateau modulus G' (Fig. S2), even though HX systems exhibit higher thiol group conversion and gel fraction. We attribute this similarity in crosslink density to their intrinsic photocuring pathways. As discussed in section 3.1, the addition of THF solvent promotes molecular-level mixing between PBD and G4, ensuring nearly full thiol group conversion in phase-mixed HX samples after photopolymerization. Meanwhile, the addition of THF also lowers the concentrations of PBD and G4, thus increasing the spatial distance between these reacting molecules during photopolymerization. This, in turn, may promote intramolecular thiol–ene reactions where a G4 molecule is covalently bonded to the same PBD chain, forming loops or other network defects that don't contribute to the overall crosslink density. In contrast, the intimate contact between dispersed G4-rich domains and neighboring PBD-rich continuous matrix in bulk could promote intermolecular thiol–ene reactions in phase-separated X samples, contributing more effectively to the overall crosslink density. Such network topology differences can help explain the comparable effective crosslink densities in these X0.5–X2 and HX0.5–HX2 networks, despite their distinct overall thiol conversions, gel fractions, and phase morphologies.

Fig. 4 displays the representative stress–strain curves of both phase-separated X0.75–X2 and phase-mixed HX0.5–HX2 PBD–G4 networks collected at room temperature (well above their T_gs and thus in the rubbery state), and the corresponding

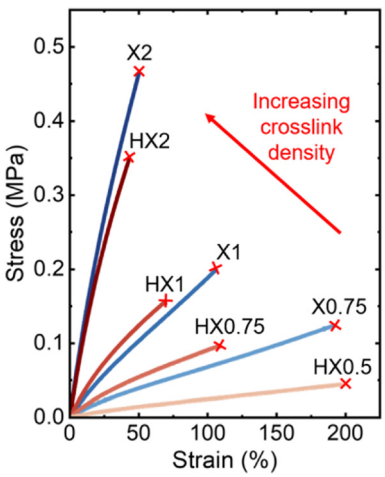

Fig. 4 Room-temperature tensile test results for photocured PBD–G4 samples with (X0.75–X2) and without (HX0.5–HX2) macroscopic phase separation at varying compositions. Note that the X0.5 film was sticky and not self-standing, thus not suitable for tensile testing.

Young's modulus, tensile strength, and elongation at break extrapolated from these curves are compiled in Table 2. (It is noteworthy that X0.5 was not subjected to tensile testing because its low G4 loading resulted in insufficient network formation and thus low gel fraction to produce a self-standing film.) As shown in Fig. 4 and Table 2, increasing G4 loading leads to a gradual increase in Young's modulus and tensile strength in both X0.75–X2 and HX0.5–HX2 networks, accompanied by a decrease in elongation at break. For example, the Young's modulus and tensile strength increased from 0.08 MPa and 0.12 MPa for X0.75 to 1.23 MPa and 0.44 MPa for X2, while the elongation at break decreased from 193% for X0.75 to 48% for X2, respectively. Similarly, the Young's modulus and tensile strength increase from 0.03 MPa and 0.05 MPa for HX0.5 to 1.13 MPa and 0.33 MPa for HX2, while the elongation at break decreased from 210% for HX0.5 to 40% for HX2, respectively. These trends can be attributed to the increase in crosslink density with increasing G4 loading observed in both separated and phase-mixed PBD–G4 network series (see section 3.1), where crosslinking enhances sample stiffness while restricting large-scale chain deformation.

It is important to note that the mechanical properties of these PBD–G4 networks are significantly lower than those of conventional rigid thermosets, such as aromatic epoxy networks, which typically exhibit T_g values in the range of 150–200 °C, rubbery plateau moduli on the order of 1–10 MPa, and tensile strengths exceeding 80 MPa.[62–64] This difference arises from the distinct network design in this study, where flexible PBD chains and disulfide-containing oligomers lead to long network strands and relatively low crosslink density. As a result, these materials behave as soft elastomers with low T_g values (−90 to −73 °C) and correspondingly low modulus and tensile strength under ambient conditions.

A one-to-one comparison between the tensile properties of phase-separated X *vs.* phase-mixed HX samples indicates that these two series of samples exhibit similar Young's modules at the same G4 loadings. This can be attributed to their nearly identical overall crosslink density as discussed in section 3.1 (Fig. 3b and Fig. S2), since the rubbery-state Young's modulus measured by tensile test is directly proportional to the E' or G' measured by DMA or rheometer. According to Fig. 4 and Table 2, the X0.75–2 series report tensile strength and elongation at break values that are consistently greater than those of the HX0.75–2 series at the same G4 loadings. We attribute these differences in their failure behaviors to their distinct network morphologies/topologies: In the phase-mixed HX samples, the solvent-induced molecular-level mixing and network swelling may result in PBD–G4 networks with extended chain conformations and thus limited overall extensibility. In the phase-separated X samples, however, the G4-rich domains dispersed within the network matrix can help redistribute stress under tension and enable more gradual deformation prior to mechanical fracture. As a result, at identical G4 loadings, the phase-separated X series exhibit consistently higher tensile strength and elongation at break than those of their corresponding phase-mixed HX series.

To further probe the time-dependent mechanical response of these networks under ambient conditions, stress relaxation experiments were performed on X2 and HX2 at room temperature under a constant strain of 5%. As shown in Fig. S6, the stress remains nearly constant over a period of 5 min for both X2 and HX2 networks, indicative of negligible stress relaxation under these conditions. These results suggest that both phase-separated and phase-mixed PBD–G4 networks behave as effectively static and elastic networks at room temperature. Consequently, any stress relaxation or creep behavior observed under ambient conditions primarily reflects their intrinsic viscoelastic response, rather than dynamic bond exchange processes.

Overall, the DSC, DMA, and tensile test results above confirm the successful synthesis of both phase-separated and single-phase PBD–G4 networks with well-controlled chemical compositions, network structures, and phase morphologies. At identical chemical compositions (*i.e.*, G4 loadings), photocuring pathway plays a key role in dictating final network structures and phase morphologies, resulting in distinct thermal and mechanical properties.

Fig. S7 compiles the TGA weight loss profiles under nitrogen for both X0.5–X2 and HX0.5–HX2 PBD–G4 networks. All samples display excellent thermal stability, exhibiting <2wt% mass loss below 250 °C. Notably, the TGA curves of HX samples show no detectable mass loss in the temperature range of 35–200 °C, confirming that all THF has been removed after a two-step drying process. Upon further heating, rapid mass loss occurs, and all samples fully decompose at temperatures above 500 °C, with negligible residue mass remaining. For both phase-separated X and phase-mixed HX series, the onset of thermal degradation systematically shifts to lower temperatures at higher G4 contents, reflecting a gradual decrease in thermal stability. This trend can be attributed to the increasing concentration of disulfide bonds with an increasing G4 loading, which possess lower bond dissociation energies than the carbon–carbon bonds in the PBD backbone and therefore undergo thermal scission at lower temperatures.[65] At identical G4 loadings, phase-separated *vs.* single-phase PBD–G4 networks exhibit nearly identical TGA weight loss profiles, indicating that thermal stability is governed primarily by chemical composition rather than curing-induced phase morphology or network topology.

3.4. Deconstruction of phase-separated *vs.* phase-mixed PBD–G4 networks

As discussed in the stress relaxation results above (Fig. S6), both X2 and HX2 exhibit minimal stress decay over time under ambient conditions. Despite the presence of disulfide bonds, the solid-state PBD–G4 networks remain effectively static at room temperature, as disulfide–disulfide exchange is negligible under such conditions.[66] Also, we note that no evidence of acetal linkage degradation was observed in these networks, consistent with the known stability of acetal groups under neutral and basic conditions in the absence of acid and moisture.[67–69] In this study, the dynamic bond exchange in

PBD–G4 networks is governed by thiol–disulfide exchange reactions associated with their embedded disulfide bonds, which are activated under elevated temperature in the presence of base catalysts and excess thiol groups.

As illustrated in Fig. 5a, the thiol–disulfide exchange reactions allow them to undergo network deconstruction upon treatment with excess thiol-containing molecules (*e.g.*, G4 in this study), in the presence of TEA as a base catalyst and toluene as a swelling solvent at ~70 °C. We first performed control experiments on the X0.5 sample having the lowest effective crosslink density, by comparing three degradation conditions: (i) addition of excess G4 only, (ii) addition of TEA only, and (iii) addition of both G4 and TEA (note: the mass ratios between X0.5 and G4 were set to 1 : 1 in both (i) and (iii)). When both G4 and TEA were added, X0.5 exhibited the fastest decrosslinking, achieving complete network deconstruction and forming a homogeneous solution within a week. In comparison, samples treated with G4 alone showed significantly slower decrosslinking, achieving only partial network decomposition after a month under identical conditions. Notably, samples treated with TEA alone showed almost no network deconstruction even after prolonged heating for a month at 70 °C. These experiments demonstrate that a combination of excess thiols and TEA base catalysts promotes the deconstruction of these disulfide-containing PBD–G4 networks through thiol–disulfide exchange reactions.

Subsequently, we performed decrosslinking experiments on both X0.5–X2 and HX0.5–HX2 PBD–G4 networks with a combination of G4 and TEA, by maintaining the mass ratios of X0.5 : G4 : TEA = 1 : 1 : 2, X0.75 : G4 : TEA = 1 : 1.5 : 3, X1 : G4 : TEA = 1 : 2 : 4, and X2 : G4 : TEA = 1 : 4 : 8 while keeping other deconstruction conditions identical. As shown in Fig. 5b, both phase-separated X0.5–X1 and phase-mixed HX0.5–HX1 networks at relatively low G4 loadings underwent complete network deconstruction, with required deconstruction time increasing from ~1 week for X0.5 to ~1 month for HX1. At higher G4 loadings, both X2 and HX2 networks underwent much slower decrosslinking and only achieved partial network deconstruction after ~2 months. These results indicate that the deconstruction rates/degrees of these PBD–G4 networks decrease with increasing crosslink density. Above a critical crosslink density, these crosslinked networks may exhibit limited network swelling and thus restrict the diffusion of deconstruction agents (*i.e.*, G4), thus exhibiting suppressed network deconstruction *via* thiol–disulfide exchange reactions.

It is also noteworthy that under identical decrosslinking conditions and chemical compositions (*i.e.*, G4 content), the deconstruction time required for phase-mixed HX series is consistently longer than that of the phase-separated X counterpart, *e.g.*, HX0.5 ≈ 1.5–2 weeks *vs.* X0.5 ≈ 1 week. Although X0.5 contains residual free thiols (~40%) due to incomplete thiol conversion, the calculated overall thiol-to-disulfide ([SH] : [S–S]) molar ratios under the applied decrosslinking conditions are nearly identical at 4.69 : 1 for X0.5 (*i.e.*, added G4 + residual thiols) and 4.53 : 1 for HX0.5 (*i.e.*, added G4). Therefore, the difference in deconstruction timescale is unlikely to originate from free thiol availability. Additionally, both networks are fully swollen in excess toluene (within an hour) before bond exchange and network deconstruction occurs (within 1–2 weeks), ensuring comparable accessibility of thiols to disulfide bonds in both X and HX systems. The deconstruction timescale thus reflects the breakdown of the remaining gel fraction after swelling, which is governed by network morphology. These results demonstrate that network structures and phase morphologies are key in dictating their deconstruction behaviors, despite the same chemical compositions. The faster network deconstruction of the X series can be attributed to the localization of the disulfide bonds (within

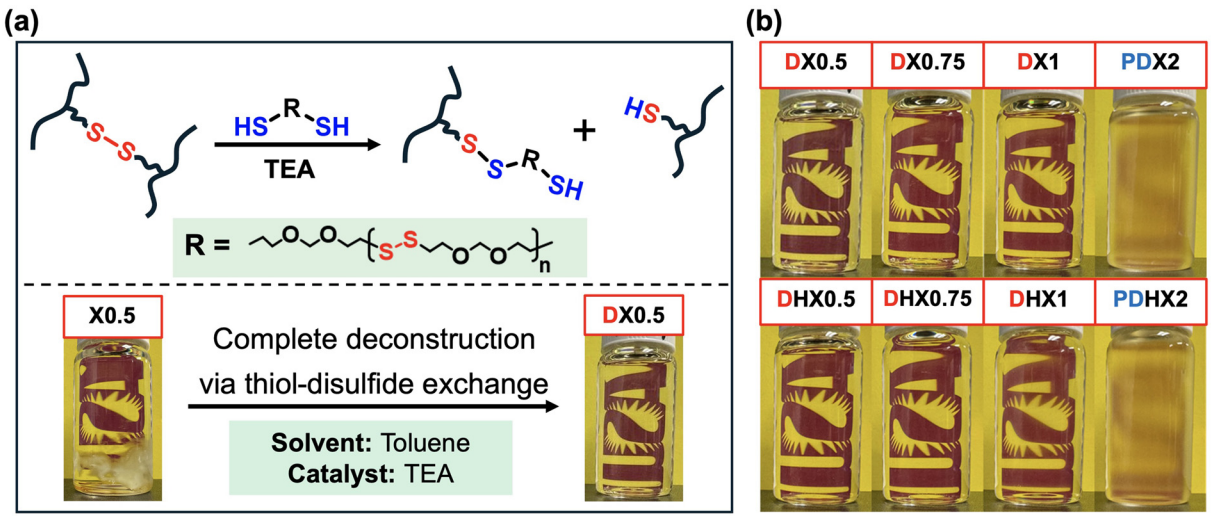

Fig. 5 (a) Reaction scheme and decrosslinking experiment showing the deconstruction of thiol–ene PBD–G4 networks through dynamic thiol–disulfide exchange reactions; (b) decrosslinking results for photocured PBD–G4 samples with (X0.5–X2) and without (HX0.5–HX2) macroscopic phase separation at varying compositions. D represents complete network deconstruction, while PD represents partial network deconstruction.

effective crosslinking strands) at or near the PBD/G4 phase boundaries and the better penetration of toluene/G4 through the continuous PBD-rich matrix.

4. Conclusions

In conclusion, morphologically distinct dynamic thiol–ene photopolymer networks, *i.e.*, phase-separated (X series) *vs.* phase-mixed (HX series) PBD-G4 networks, were successfully prepared from thermodynamically incompatible PBD and Thioplast G4 at identical chemical compositions. Phase-separated X network series, obtained *via* bulk PBD and G4 mixing and then photocuring, feature G4-rich domains dispersed within a PBD-rich continuous matrix, exhibiting incomplete thiol conversion, two separate T_gs, relatively large elongation at break, and facile network deconstruction. In direct comparison, phase-mixed HX network series, prepared by photocuring PBD/G4/THF mixtures in the solution state, showed full thiol conversion, a single T_g, reduced elongation at break, and slower network deconstruction kinetics than the X counterparts, despite the comparable crosslink densities in both X and HX series. Systematic variation of G4 content effectively tunes the crosslink density in both network series without interfering with their phase behavior, leading to increased gel fraction, T_g, and mechanical stiffness, but reduced extensibility and slower network deconstruction with increasing G4 loading. Overall, these results establish phase morphology as a powerful design parameter for programming the structure, thermomechanical performance, and recyclability of dynamically crosslinked thiol–ene photopolymer networks comprising disulfide bonds.

Author contributions

Mengdi Chen: conceptualization, methodology, validation, writing – original draft, writing – review and editing; Reyna Stockwell: methodology, validation, writing – original draft, writing – review and editing; Saleh Alfarhan: methodology; Kailong Jin: conceptualization, validation, funding acquisition, supervision, project administration, writing – review and editing.

Conflicts of interest

There are no conflicts of interest to declare.

Data availability

The data supporting this article have been included as part of the supplementary information (SI). Supplementary information: Fig. S1–S7, NMR spectra and further experimental details. See DOI: https://doi.org/10.1039/d6lp00028b.

Acknowledgements

The authors acknowledge the startup research funding support provided by the Ira A. Fulton Schools of Engineering at Arizona State University (ASU), National Science Foundation (NSF-2338613), and Air Force Office of Scientific Research (AFOSR-FA9550-25-1-0189). The authors also acknowledge the Biodesign Center for Sustainable Macromolecular Materials and Manufacturing at ASU for the access and use of shared facilities. Moreover, the authors acknowledge the Magnetic Resonance Research Center, part of the Chemical and Environmental Characterization Core Facilities at Arizona State University.

References

1 F. Jasinski, A. Rannée, J. Schweitzer, D. Fischer, E. Lobry, C. Croutxé-Barghorn, M. Schmutz, D. Le Nouen, A. Criqui and A. Chemtob, *Macromolecules*, 2016, **49**, 1143–1153.
2 D. P. Nair, N. B. Cramer, T. F. Scott, C. N. Bowman and R. Shandas, *Polymer*, 2010, **51**, 4383–4389.
3 H. Fang and C. A. Guymon, *Polym. Int.*, 2022, **71**, 596–607.
4 B. D. Fairbanks, T. F. Scott, C. J. Kloxin, K. S. Anseth and C. N. Bowman, *Macromolecules*, 2009, **42**, 211–217.
5 M. Topa-Skwarczyńska and J. Ortyl, *Polym. Chem.*, 2023, **14**, 2145–2158.
6 O. Llorente, A. Agirre, I. Calvo, M. Olaso, R. Tomovska and H. Sardon, *Polym. J.*, 2021, **53**, 1195–1204.
7 A. K. O'Brien, N. B. Cramer and C. N. Bowman, *J. Polym. Sci., Part A:Polym. Chem.*, 2006, **44**, 2007–2014.
8 S. C. Ligon, B. Husár, H. Wutzel, R. Holman and R. Liska, *Chem. Rev.*, 2014, **114**, 557–589.
9 C. C. Cook, E. J. Fong, J. J. Schwartz, D. H. Porcincula, A. C. Kaczmarek, J. S. Oakdale, B. D. Moran, K. M. Champley, C. M. Rackson, A. Muralidharan, R. R. McLeod and M. Shusteff, *Adv. Mater.*, 2020, **32**, 2003376.
10 C. E. Hoyle and C. N. Bowman, *Angew. Chem., Int. Ed.*, 2010, **49**, 1540–1573.
11 Z. Li, Z. Xu, S. Propst, Z. A. Page, Y. Chen, C. Majidi and J. Mueller, *Adv. Mater. Technol.*, 2025, **10**, e00422.
12 A. Navaruckiene, S. Kasetaite and J. Ostrauskaite, *Rapid Prototyp. J.*, 2019, **26**, 402–408.
13 M. Podgórski, S. Huang and C. N. Bowman, *ACS Appl. Mater. Interfaces*, 2021, **13**, 12789–12796.
14 R. Becker, A. S. Kuenstler and C. N. Bowman, *Dent. Mater.*, 2024, **40**, 976–983.
15 G. Zhu, H. A. Houck, C. A. Spiegel, C. Selhuber-Unkel, Y. Hou and E. Blasco, *Adv. Funct. Mater.*, 2024, **34**, 2300456.
16 Y. Hu, B. A. Kowalski, S. Mavila, M. Podgórski, J. Sinha, A. C. Sullivan, R. R. McLeod and C. N. Bowman, *ACS Appl. Mater. Interfaces*, 2020, **12**, 44103–44109.
17 M. Alrefai and M. Maric, *RSC Adv.*, 2025, **15**, 312–322.
18 J. Bai, H. Li, Z. Shi and J. Yin, *Macromolecules*, 2015, **48**, 3539–3546.

19 Z. Wang, H. Liang, H. Yang, L. Xiong, J. Zhou, S. Huang, C. Zhao, J. Zhong and X. Fan, *Prog. Org. Coat.*, 2019, **137**, 105282.
20 J. J. Hernandez, A. L. Dobson, B. J. Carberry, A. S. Kuenstler, P. K. Shah, K. S. Anseth, T. J. White and C. N. Bowman, *Macromolecules*, 2022, **55**, 1376–1385.
21 A. S. Kuenstler, J. J. Hernandez, M. Trujillo-Lemon, A. Osterbaan and C. N. Bowman, *ACS Appl. Mater. Interfaces*, 2023, **15**, 11111–11121.
22 J. J. Hernandez, S. P. Keyser, A. L. Dobson, A. S. Kuenstler and C. N. Bowman, *Macromolecules*, 2024, **57**, 1426–1437.
23 R. Korotkov, J. V. Tumaneng, R. Bongiovanni, S. Dalle Vacche, E. Rossegger and S. Schlögl, *Macromol. Rapid Commun.*, 2025, **46**, e00654.
24 T. E. Brown, B. J. Carberry, B. T. Worrell, O. Y. Dudaryeva, M. K. McBride, C. N. Bowman and K. S. Anseth, *Biomaterials*, 2018, **178**, 496–503.
25 M. Podgórski, N. Spurgin, S. Mavila and C. N. Bowman, *Polym. Chem.*, 2020, **11**, 5365–5376.
26 C. Wang, T. M. Goldman, B. T. Worrell, M. K. McBride, M. D. Alim and C. N. Bowman, *Mater. Horiz.*, 2018, **5**, 1042–1046.
27 H. Gao, Y. Sun, M. Wang, B. Wu, G. Han, L. Jin, K. Zhang and Y. Xia, *Polymer*, 2021, **212**, 123132.
28 S. Alfarhan, J. Brown, B. Liu, T. Long and K. Jin, *J. Polym. Sci.*, 2022, **60**, 3379–3390.
29 S. Alfarhan, J. Nettles, P. Prabhudesai, J.-C. Yu, C. Westover, T. Tang, W. Wang, X. Chen, S. E. Seo, X. Li, T. E. Long and K. Jin, *Polym. Chem.*, 2024, **15**, 1141–1151.
30 S. Alfarhan, M. Chen, J. Huish and K. Jin, *Small*, 2025, **21**, 2505122.
31 Y. Hu, S. M. Soars, B. E. Kirkpatrick, M. Podgorski, N. Bongiardina, B. D. Fairbanks, K. S. Anseth and C. N. Bowman, *Macromolecules*, 2023, **56**, 9778–9786.
32 S. M. Soars, N. J. Bongiardina, B. D. Fairbanks, M. Podgórski and C. N. Bowman, *Macromolecules*, 2022, **55**, 1811–1821.
33 H. Alzubi, S. Moradi, O. Konuray, X. Fernández-Francos and X. Ramis, *Polym. Test.*, 2025, **147**, 108800.
34 W. Alabiso, B. Sölle, D. Reisinger, G. Guedes, de la Cruz, M. Schmallegger, T. Griesser, E. Rossegger and S. Schlögl, *Angew. Chem., Int. Ed.*, 2023, **62**, e202311341.
35 G. B. Lyon, L. M. Cox, J. T. Goodrich, A. D. Baranek, Y. Ding and C. N. Bowman, *Macromolecules*, 2016, **49**, 8905–8913.
36 M. Ge, Y. Li, L. Wu, R. Liu and J.-T. Miao, *Macromolecules*, 2024, **57**, 2394–2402.
37 H. Niu, Y. Li, P. Zhang, W. Guo, X. Wang and Y. Hu, *Polym. Chem.*, 2024, **15**, 4952–4961.
38 L. D. Dugas, W. D. Walker, R. Shankar, K. S. Hoppmeyer, T. L. Thornell, S. E. Morgan, R. F. Storey, D. L. Patton and Y. C. Simon, *Macromol. Rapid Commun.*, 2022, **43**, 2200249.
39 M. Ahmadi, K. Ehrmann, M. Göschl, P. Schlossgangl, T. Koch, R. Liska and J. Stampfl, *J. Appl. Polym. Sci.*, 2025, **142**, e57404.
40 M. Wang, P. Zhang, M. Shamsi, J. L. Thelen, W. Qian, V. K. Truong, J. Ma, J. Hu and M. D. Dickey, *Nat. Mater.*, 2022, **21**, 359–365.
41 L. Zhang, S. Wang, Z. Wang, Z. Liu, X. Xu, H. Liu, D. Wang and Z. Tian, *ACS Nano*, 2023, **17**, 13948–13960.
42 Z. Wang, W. Qiu and Q. Zhang, *Prog. Polym. Sci.*, 2024, **154**, 101847.
43 O. Okay, *Polymer*, 1999, **40**, 4117–4129.
44 W. Oh, J.-S. Bae and J.-W. Park, *Macromolecules*, 2021, **54**, 1192–1202.
45 M. H. P. De Heer Kloots, S. K. Schoustra, J. A. Dijksman and M. M. J. Smulders, *Soft Matter*, 2023, **19**, 2857–2877.
46 G. Zhang, J. Steck, J. Kim, C. H. Ahn and Z. Suo, *Sci. Adv.*, 2023, **9**, eadh7742.
47 L. Zakrzewski, K. D. Purkaysta, C. Bae and C. R. Picu, *ACS Appl. Polym. Mater.*, 2024, **6**, 5028–5038.
48 X. Ming, L. Yao, H. Zhu, Q. Zhang and S. Zhu, *Adv. Funct. Mater.*, 2022, **32**, 2109850.
49 L. Chen, C. Zhao, J. Huang, J. Zhou and M. Liu, *Nat. Commun.*, 2022, **13**, 6821.
50 Z. Xing, Z. Wang, X. Zhao and X. Yang, *ACS Appl. Polym. Mater.*, 2024, **6**, 8687–8696.
51 H. Han and X. Xu, *J. Appl. Polym. Sci.*, 2018, **135**, 46307.
52 T. Kito and M. Hayashi, *Soft Matter*, 2024, **20**, 2961–2968.
53 H. Fang, X. Gao, F. Zhang, W. Zhou, G. Qi, K. Song, S. Cheng, Y. Ding and H. H. Winter, *Macromolecules*, 2022, **55**, 10900–10911.
54 L. M. A. Joosten, P. Cassagnau, E. Drockenmuller and D. Montarnal, *Adv. Funct. Mater.*, 2024, **34**, 2306882.
55 K. M. Herbert, P. T. Getty, N. D. Dolinski, J. E. Hertzog, D. de Jong, J. H. Lettow, J. Romulus, J. W. Onorato, E. M. Foster and S. J. Rowan, *Chem. Sci.*, 2020, **11**, 5028–5036.
56 N. D. Dolinski, R. Tao, N. R. Boynton, A. P. Kotula, C. A. Lindberg, K. J. Petersen, A. M. Forster and S. J. Rowan, *ACS Macro Lett.*, 2024, **13**, 174–180.
57 E. G. Hanna, K. Younes, S. Amine and R. Roufayel, *Gels*, 2023, **9**, 828.
58 H. H. Winter and F. Chambon, *J. Rheol.*, 1986, **30**, 367–382.
59 C. Chen, Y. Xu, Y. Chen, C. M. Evans and P. V. Braun, *ACS Macro Lett.*, 2025, **14**, 687–694.
60 H. M. James and E. Guth, *J. Chem. Phys.*, 1943, **11**, 455–481.
61 I. M. Kalogeras and W. Brostow, *J. Polym. Sci., Part B: Polym. Phys.*, 2009, **47**, 80–95.
62 F.-L. Jin, X. Li and S.-J. Park, *J. Ind. Eng. Chem.*, 2015, **29**, 1–11.
63 M. Liang, X. Liu, D. Liu, X. Li, X. Hu, C. Feng, T.-T. Li, J.-H. Lin, B. Chang and J. Chen, *J. Polym. Res.*, 2024, **31**, 337.
64 G. Gibson, in *Brydson's Plastics Materials*, Elsevier, 2017, pp. 773–797.
65 R. Steudel, *Angew. Chem., Int. Ed. Engl.*, 1975, **14**, 655–664.
66 M. Pepels, I. Filot, B. Klumperman and H. Goossens, *Polym. Chem.*, 2013, **4**, 4955–4965.
67 N. Kongkatigumjorn and D. Crespy, *Polym. Chem.*, 2024, **15**, 4491–4518.
68 H. Cao, Y. Dong, L. Bre, C. Tapeinos, W. Wang and A. Pandit, *RSC Adv.*, 2016, **6**, 9604–9611.
69 A. Hufendiek, S. Lingier and F. E. D. Prez, *Polym. Chem.*, 2019, **10**, 9–33.